Crystal electric field excitations in the quasicrystal approximant $TbCd_6$ studied by inelastic neutron scattering

Pinaki Das,[1,2] P.-F. Lory,[3] R. Flint,[1,2] T. Kong,[1,2] T. Hiroto,[4] S. L. Bud'ko,[1,2] P. C. Canfield,[1,2] M. de Boissieu,[3] A. Kreyssig,[1,2] and A. I. Goldman[1,2]

[1]*Ames Laboratory, U. S. DOE, Iowa State University, Ames, Iowa 50011, USA*

[2]*Department of Physics and Astronomy, Iowa State University, Ames, Iowa 50011, USA*

[3]*University of Grenoble Alpes, CNRS, SIMAP, 38000 Grenoble, France*

[4]*Department of Materials Science and Technology, Tokyo University of Science, Noda, JP-278-8510, Japan*

(Received 19 November 2016; published 7 February 2017)

We have performed inelastic neutron scattering measurements on powder samples of the quasicrystal approximant, $TbCd_6$, grown using isotopically enriched ^{112}Cd. Both quasielastic scattering and distinct inelastic excitations were observed below 3 meV. The intensity of the quasielastic scattering measured in the paramagnetic phase diverges as $T_N \sim 22$ K is approached from above. The inelastic excitations, and their evolution with temperature, are well characterized by the leading term, $B_2^0 O_2^0$, of the crystal electric field (CEF) level scheme for local pentagonal symmetry for the rare-earth ions [S. Jazbec *et al.*, Phys. Rev. B **93**, 054208 (2016)] indicating that the Tb moment is directed primarily along the unique local pseudofivefold axis of the Tsai-type clusters. We also find good agreement between the inverse susceptibility determined from magnetization measurements using a magnetically diluted $Tb_{0.05}Y_{0.95}Cd_6$ sample and that calculated using the CEF level scheme determined from the neutron measurements.

DOI: 10.1103/PhysRevB.95.054408

I. INTRODUCTION

The quasicrystal approximants, RCd_6 (R = rare earth) [1,2], and related icosahedral quasicrystal phases, i-R-Cd [3], form a set of model systems to explore how magnetism evolves from a conventional periodic lattice (approximant phase) to an aperiodic quasicrystal. Although $TbCd_6$ manifests long-range antiferromagnetic order ($T_N \sim 22$ K) [4–6], only spin-glass-like behavior is observed in i-Tb-Cd with a spin freezing temperature of $T_F = 6$ K [3,7]. In fact, all of the known quasicrystals with local moments exhibit spin-glass-like ground states at low temperature [8,9].

The origin of the differences in magnetic behavior between the periodic approximants and quasicrystalline phases remain an open and intriguing issue, especially in light of the fact that numerous theoretical studies have established that long-range magnetic order on a quasilattice is quite possible [10–16]. Nevertheless, there are differences between the local environments surrounding the R ions in the approximant and quasicrystalline structures. The 1/1-RCd_6 approximants may be described, at ambient temperature, as a body-centered cubic packing of interpenetrating rhombic triacontahedron (RTH) Tsai-type clusters [1,17], featuring an icosahedron of 12 R ions comprising the third shell of each cluster. These clusters are linked along the cubic axes by sharing a face, and interpenetrate neighboring clusters along the body diagonal. For i-R-Cd quasicrystals, however, $\sim$ 60–70% of the R ions are associated with the R icosahedron within the Tsai-type cluster, and the balance are contained within the double Friauf polyhedron (DFP) that fill the gaps between the clusters [18,19]. Furthermore, a recent 6D structural refinement of the i-R-Cd quasicrystals (R = Gd, Dy, and Tm) noted a degree of chemical disorder on the nominally R icosahedron itself [19]. Nevertheless, a comprehensive understanding of the nature of magnetism in the RCd_6 approximants provides an important starting point for elucidating the magnetic interactions in the corresponding quasicrystals. In particular, for magnetic R ions, investigations of the crystal electric field (CEF) through inelastic neutron scattering can reveal key information regarding the local magnetism of the R ions and the orientation of the magnetic moments relative to the local structure.

II. EXPERIMENTAL DETAILS

$TbCd_6$ single crystals were synthesized using a high-temperature solution growth technique [3,7,20,21]. The starting elements (Tb: Ames Laboratory Material Preparation Center; Cd: ^{112}Cd from Cambridge Isotope Laboratories) were packed in a frit-disk crucible set [22] with a molar ratio Tb:Cd = 7:93, which were then sealed in a silica tube under partial Ar atmosphere. The ampoule was heated to 700 °C to realize a homogeneous liquid and slowly cooled to 500 °C over $\sim$130 h. The remaining Cd solution was separated from $TbCd_6$ single crystals at 500 °C in a centrifuge. The samples were annealed for one week at 200 °C and were then finely grounded for the inelastic neutron scattering measurements. dc magnetization data down to 2 K were measured on a single crystal of $Y_{0.95}Tb_{0.05}Cd_6$ ($m \sim 0.143$ g), using a Quantum Design (QD) magnetic property measurement system (MPMS), superconducting quantum interference device (SQUID) magnetometer (T = 1.8–300 K; H = 0.05 T).

The inelastic neutron scattering measurements were performed on the IN4 spectrometer at the Institut Laue-Langevin, France, using the $TbCd_6$ polycrystalline samples with a total mass of $\sim$ 2.4 g contained in a cylindrical vanadium sample holder. The sample was cooled in an orange-type cryostat and measurements were performed using a constant incident neutron wavelength of 3 Å ($E_i = 9.3$ meV), with an energy resolution of $\sim$ 0.4 meV determined from the width of the incoherent scattering. $TbCd_6$ undergoes two

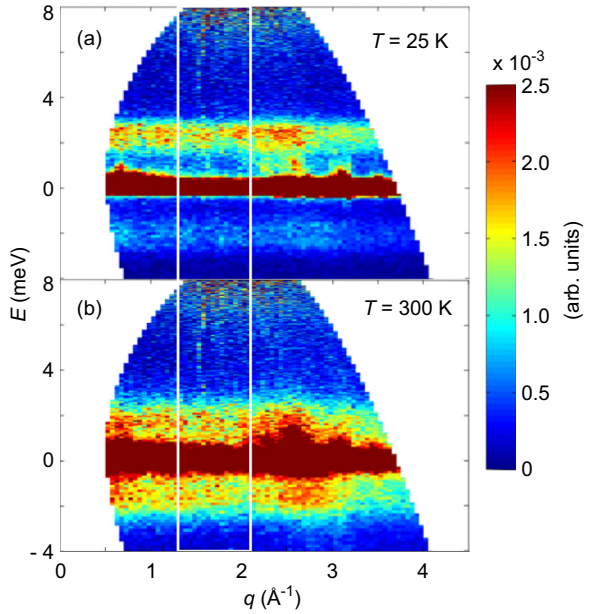

FIG. 1. Inelastic neutron scattering spectrum obtained from polycrystalline $TbCd_6$ samples at (a) $T = 25$ K and (b) $T = 300$ K. Data were taken at IN4 spectrometer using an incident neutron wavelength of 3 Å ($E_i = 9.3$ meV). Detailed analysis of the spectra was done over the q-range bounded by the white vertical lines.

consecutive antiferromagnetic transitions below $T_{N1} \sim 22$ K and $T_{N2} \sim 17.5$ K [4,6]. All data presented here were taken in the paramagnetic phase above T_{N1}.

III. RESULTS AND DISCUSSION

Figures 1(a) and 1(b) show the inelastic neutron scattering spectra obtained at the IN4 spectrometer at $T = 25$ K and 300 K, respectively. The data are presented in the form of a color map where the scattering intensity, $S(q,E)$, is plotted as a function of neutron energy transfer, E, and the magnitude of the scattering vector, $q = |q|$. In addition to the intense elastic scattering at $E = 0$ meV, we observe a flat band of inelastic scattering centered at ~2 meV associated with CEF excitations. No additional scattering is observed above ~3 meV suggesting a limit on the maximum energy transfer for the CEF transitions. We do observe additional dispersive scattering at higher q, which increases strongly with increasing temperature, characteristic of scattering from phonons. Therefore, in order to accurately evaluate the scattering from CEF excitations, data were summed and analyzed over a restricted range in q as indicated by the white lines in Fig. 1.

A. Fitting the data

A total of six temperature data sets ($T = 25$,50, 150,175,225, and 300 K) above T_{N1} were measured and analyzed. Figure 2 shows the neutron scattering intensities, integrated over the q range, $1.3 \leqslant q \leqslant 2.1$ Å^{-1}, plotted as a function of the neutron energy transfer, E, at $T = 25$, 150, and 300 K. The scattering, $S(E)$, at all temperatures is comprised of three contributions that include (i) the elastic

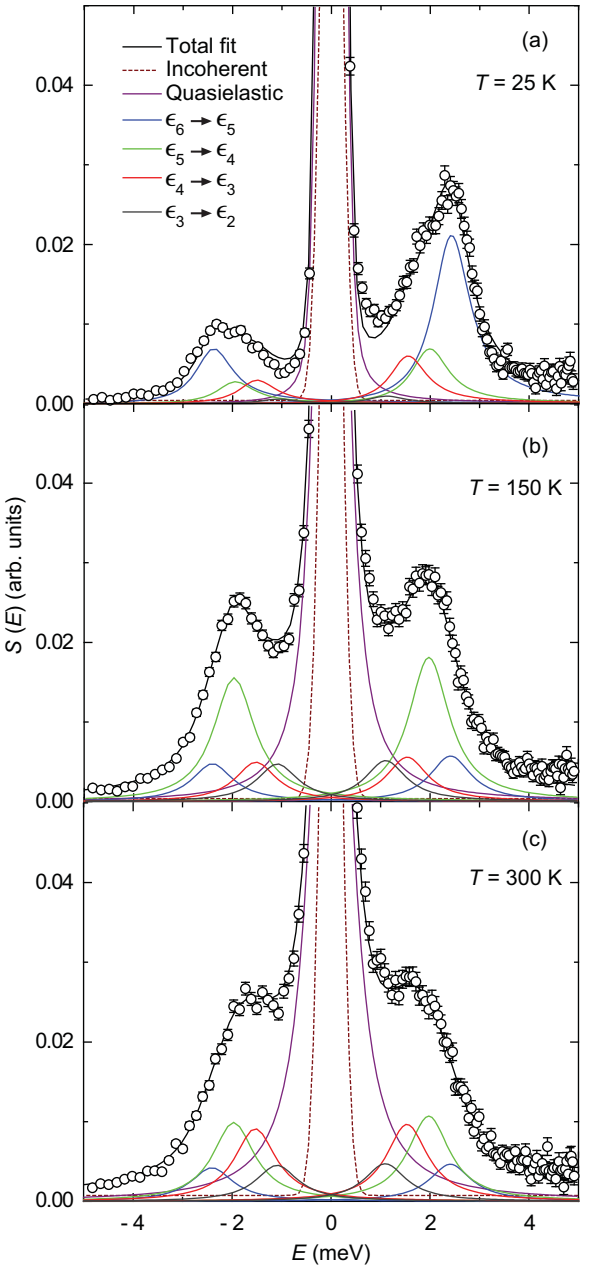

FIG. 2. Neutron scattering intensity integrated over the q range from 1.3 to 2.1 Å^{-1}, as a function of the neutron energy transfer, E, at temperatures (a) $T = 25$ K, (b) $T = 150$ K, and (c) $T = 300$ K. The fits to the data are described in the text.

incoherent scattering fit using a simple Gaussian function at $E = 0$ meV, (ii) the quasielastic magnetic scattering fit using a Voigt function centered at $E = 0$ meV, and (iii) the inelastic scattering arising from the CEF excitations fit using Lorentzian functions centered at the energy transfer corresponding to the CEF excitations:

$$S(E) = S(E)_{INC} + S(E)_{QE} + S(E)_{CEF}, \quad (1)$$

$$S(E)_{CEF} = \sum_{ij} \frac{\chi_{ij}(T)}{1 - e^{(-\hbar\omega/k_B T)}} \frac{1}{2\pi} \frac{\hbar\omega\gamma(T)}{(\hbar\omega - \epsilon_{ij})^2 + \frac{\gamma(T)^2}{4}}, \quad (2)$$

where $\chi_{ij}(T)$ describes the temperature dependence of the susceptibility and is proportional to the matrix element for transitions between the CEF levels, k_B is the Boltzmann constant, $\gamma(T)$ is the full width at half maximum (FWHM) of the inelastic peaks, and ϵ_{ij} is the peak position corresponding to the energy for the CEF transition, $\epsilon_i \rightarrow \epsilon_j$. Each of the CEF transitions contribute to both the energy-loss ($+\epsilon_{ij}$) and energy-gain ($-\epsilon_{ij}$) sides of the inelastic spectra in Fig. 2. In our fits, $\gamma(T)$ was fixed to be the same for all inelastic peaks but was allowed to vary for different temperatures.

The temperature-independent elastic incoherent scattering was fit by a Gaussian function parametrized by an integrated intensity and full width at half maximum (FWHM), w_G, characterizing the energy resolution of the instrument (~0.4 meV). The Voigt function used to fit the quasielastic scattering includes a temperature dependent amplitude and peak widths, w_L and w_G, that describe the Lorentzian and Gaussian contributions, respectively; w_G was constrained to the same value as that for the incoherent scattering. The final results were obtained by fitting all the six data sets simultaneously. Examples of fits to the data at $T = 25$, 150, and 300 K, including all of the contributions discussed above, are shown in Fig. 2.

B. Temperature dependence of the quasielastic scattering

The results of fits to the quasielastic scattering as a function of temperature are shown in Fig. 3(a) and the corresponding integrated intensities are shown in Fig. 3(b). As expected, the intensity of the quasielastic scattering diverges as the Néel temperature, $T_{N1} \sim 22$ K, is approached from above. This is also reflected in the strong decrease in the Lorentzian contribution to the peak width, w_L of the Voigt function [Fig. 3(c)], demonstrating the increase in the spin-relaxation time. The Gaussian widths (w_G) represent the experimental resolution and were fixed to the width of the measured incoherent scattering.

C. CEF level schemes for $TbCd_6$

We first review the local environment of the Tb^{3+} ions in $TbCd_6$. At ambient temperature, $TbCd_6$ is a 1/1 cubic approximant to the binary quasicrystal i-Tb-Cd quasicrystal which can be viewed as a body-centered-cubic (bcc) packing of partially interpenetrating Tsai-type clusters (space group $I\bar{3}m$). The Tsai-type clusters are composed of five shells: the innermost region of the cluster contains a disordered tetrahedron of 4 Cd atoms, the second shell is a dodecahedron of 20 Cd atoms, the third shell consists of 12 Tb atoms located at the vertices of an icosahedron, the fourth shell is a icosidodecahedron of 30 Cd atoms, and the outermost shell is a rhombic triacontahedron of 60 Cd atoms [1,17,23]. The Tb atoms are located at the 24(g) Wyckoff sites along the pseudofivefold axes of the cluster and are surrounded by Cd arranged in a distorted monocapped double pentagonal antiprism as shown in Fig. 4 [1,2]. In this high temperature cubic phase the innermost Cd tetrahedra are disordered with each taking on one of three orientations within the Tsai cluster. Therefore, the Cd ion site denoted by the light blue atom in Fig. 4 has an occupancy of $\frac{1}{3}$.

Below $T_S \sim 190$ K, $TbCd_6$ undergoes a small monoclinic distortion associated with the ordering of the innermost Cd tetrahedra in the Tsai clusters [24,25]. The low temperature phase [26] is isostructural to icosahedral Zn-Sc [27,28] with

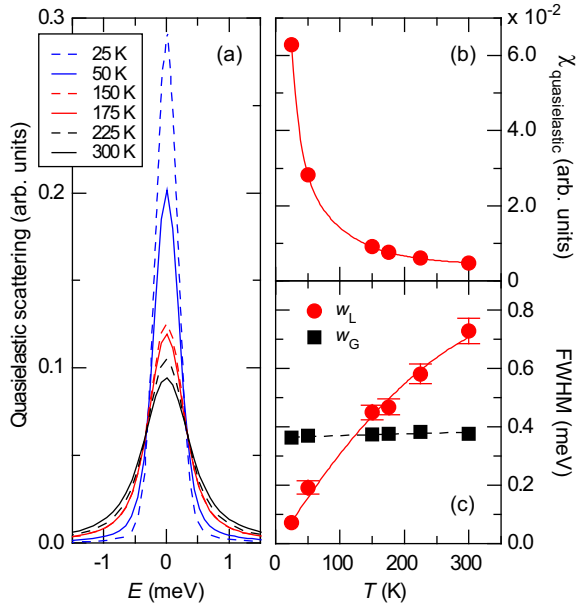

FIG. 3. Temperature dependence of the quasielastic scattering. Panel (a) shows the fits and the corresponding integrated intensities and peak width parameters are shown in panels (b) and (c), respectively. The Gaussian (w_G) contribution to the FWHM of the Voigt function was fixed to the value obtained from fits to the incoherent scattering.

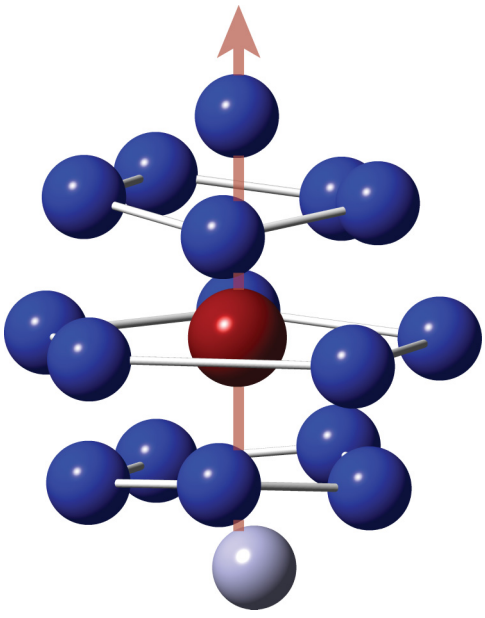

FIG. 4. Tb^{3+} (red atom) nearest neighbor coordination shell in $TbCd_6$. The R ion is surrounded by 16 Cd (dark blue atoms) forming a monocapped, double, pentagonal antiprism. The light blue atom below the inner pentagonal plane has an occupancy of $\frac{1}{3}$ in the high temperature cubic phase. The line and arrow denote the unique axis of the polyhedron.

the central tetrahedron distorting the icosahedral symmetry of successive shells. As a result, the Tb^{3+} ions now occupy six sites rather than a single site with further distortions of the pentagonal planes and changes in coordination. Two of the Tb^{3+} sites have a single Cd atom capping the inner pentagonal layer with C17 coordination (Fig. 4), whereas the four remaining Tb^{3+} sites are characterized by C16 coordination. The pentagonal planes themselves become somewhat more puckered, although the unique axis shown in Fig. 4 is still very much in evidence. The distortions of the local environment in the low temperature monoclinic phase will most likely lead to slight shifts in the CEF energies, broadening the observed inelastic excitations. It should be pointed out that a similar distortion, due to the central tetrahedron, most likely takes place in the high temperature phase, although dynamically, with a time scale of a few ps as evidenced in the Zn-Sc approximant [29].

Although the full CEF Hamiltonian contains many terms, in a recent study Jazbec *et al.* [30] successfully employed an approximate Hamiltonian, $H_{\rm CEF}^{(5)}$, for an idealized pentagonal local environment of the Tm^{3+} ions in the isostructural 1/1 Zn-Sc-Tm cubic approximant to model specific heat measurements. $H_{\rm CEF}^{(5)}$ can be written in terms of the Steven's operators, O_n^m, and total angular momentum operators $(J_z, J_\pm)$ as

$$H_{\rm CEF}^{(5)} = B_2^0 O_2^0 + B_4^0 O_4^0 + B_6^0 O_6^0 + B_6^5 O_6^5, \tag{3}$$

where

$$O_2^0 = 3J_z^2 - J(J+1), \tag{4}$$

$$O_4^0 = 35J_z^4 - [30J(J+1) - 25]J_z^2 - 6J(J+1) + 3J^2(J+1)^2, \tag{5}$$

$$O_6^0 = 231J_z^6 - 105[3J(J+1) - 7]J_z^4 + [105J^2(J+1)^2 - 525J(J+1) + 294]J_z^2 - 5J^3(J+1)^3 + 40J^2(J+1)^2 - 60J(J+1), \tag{6}$$

$$O_6^5 = \frac{1}{4}[J_z(J_+^5 + J_-^5) + (J_+^5 + J_-^5)J_z]. \tag{7}$$

$H_{\rm CEF}^{(5)}$ is a function of four coefficients, B_2^0, B_4^0, B_6^0, and B_6^5 which, in turn, depend upon the distance, R_j, of the jth charge from the R ion: $B_2^0 \propto R_j^{-3}$, $B_4^0 \propto R_j^{-5}$, and $B_6^0, B_6^5 \propto R_j^{-7}$.

1. CEF scheme for local icosahedral symmetry

For a local environment with true icosahedral symmetry, following the works of Walter [31,32] and Jazbec *et al.* [30], the terms involving B_2^0 and B_4^0 vanish, and the CEF Hamiltonian can be rewritten as

$$H_{\rm CEF}^{\rm ico} = B_6\left(O_6^0 - 42O_6^5\right), \tag{8}$$

The coefficient, B_6, is the lone CEF parameter governing the energy-level scheme, which merely stretches the energy ladder, or inverts it for negative B_6 values. Figure 5(a) shows the icosahedral CEF level scheme for positive B_6 values which has Γ_1 as the singlet ground state, followed by a triplet Γ_2, pentet Γ_5, and a quartet Γ_4 as the higher excited states,

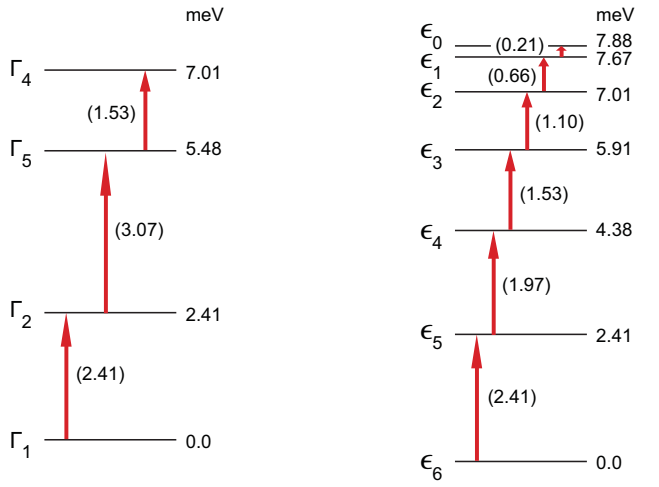

FIG. 5. CEF level schemes for icosahedral and pentagonal symmetries are shown in panels (a) and (b), respectively. With respect to the ground state, the energies of each excited energy level are shown. The allowed transitions are indicated by arrows along with the corresponding transition energies within the brackets.

using the nomenclature of Refs. [31,32]. To determine the energies of the CEF levels, we need to first determine the energy corresponding to the first excited state obtained from fits to our neutron scattering data in Fig. 2, described below. Here we note that the excitation at $E = 2.41$ meV represents a transition from the ground state to the first excited state ($\Gamma_1 \rightarrow \Gamma_2$), setting the energy scale. With this constraint, one can then calculate the energies corresponding to the transitions, $\Gamma_2 \rightarrow \Gamma_5$ and $\Gamma_5 \rightarrow \Gamma_4$, which are determined to be 3.07 and 1.53 meV, respectively. The fitted value for the B_6 parameter was 5.8×10^{-6} meV.

There are two clear discrepancies between our data and the resulting icosahedral CEF level scheme. First, we do not observe any excitation corresponding to 3.07 meV ($\Gamma_2 \rightarrow \Gamma_5$) at 300 K as evident from Fig. 2(c), where all excitations are equally probed. Secondly, the ground state cannot be a CEF singlet, since the system orders antiferromagnetically at lower temperature [6,33]. One can also consider a negative value for B_6 and invert the CEF scheme such that the quartet Γ_4 is the ground state. In that case, the transition to the first excited state, $\Gamma_4 \rightarrow \Gamma_5$, would be attributed to the 2.41 meV excitation and the higher transitions, $\Gamma_5 \rightarrow \Gamma_2$ and $\Gamma_2 \rightarrow \Gamma_1$, are expected to be at 4.82 and 3.78 meV, respectively. This again contradicts the neutron scattering data mentioned above, where no excitations above 3 meV are observed even at 300 K. We conclude that, as one would expect for the local environment surrounding the Tb^{3+} ions as shown in Fig. 4, the icosahedral CEF level scheme is not a good approximation for $TbCd_6$.

2. CEF scheme for local pentagonal symmetry

Returning to the case of local pentagonal symmetry, and following Jazbec *et al.* [30], we consider only the leading $B_2^0 O_2^0$ term in the pentagonal CEF Hamiltonian based on the rapid decrease of the higher order terms with R_j. The energy

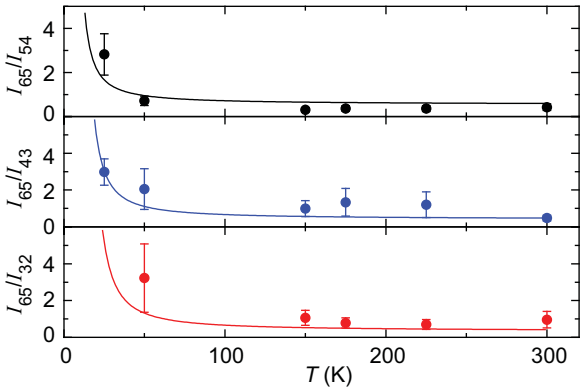

FIG. 6. Temperature dependence of the ratios of the intensities assigned to the CEF transitions. The solid lines represent the calculated ratios obtained for the pentagonal CEF level scheme.

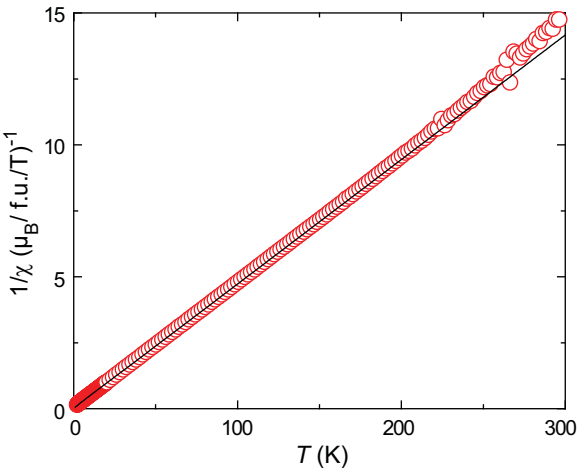

FIG. 7. Temperature dependence of the inverse magnetic susceptibility for $Y_{0.95}Tb_{0.05}Cd_6$. The solid line shows the calculated values obtained for the pentagonal CEF level scheme.

levels are determined by the matrix elements of Eq. (3) and, for $B_2^0 < 0$, there are six doubly degenerate levels, ϵ_i ($i = 1,\ldots,6$), and the singlet ϵ_0 as shown in Fig. 5(b). For $B_2^0 > 0$, the CEF level scheme in Fig. 5(b) is inverted. As before, once the energy of the first excited level is set, the energies of all levels are fixed.

From the joint refinement of the data at all temperatures using Eq. (1) and the pentagonal CEF level scheme we find a value for B_2^0 of $-0.073(1)$ meV, and the transition to the first excited state, ϵ_{65}, corresponds to an energy difference of 2.41(4) meV. With the energy of the first excited state set, the remaining CEF transitions correspond to energy differences: $\epsilon_{54} = 1.97(3)$ meV, $\epsilon_{43} = 1.53(3)$ meV, $\epsilon_{32} = 1.10(2)$ meV, $\epsilon_{21} = 0.66(2)$ meV, and $\epsilon_{10} = 0.22(2)$ meV. As demonstrated by the fits in Fig. 2 and the temperature dependence of the ratio of the measured intensities in Fig. 6, the measured data are reasonably described using only the leading axial term, $B_2^0 O_2^0$, of the pentagonal CEF level scheme. This, in turn, means that the Tb moment is directed primarily along the unique axis of the monocapped double pentagonal antiprism as shown in Fig. 4 (pseudofivefold axes) of the Tsai-type clusters. The determined values for the energy FWHM of the excitations, $\gamma(T)$, at all temperatures were nearly constant at a value of 1.0(2) meV, significantly broader than the resolution of the instrument and consistent with distortions of the local environment away from ideal pentagonal symmetry. Interestingly, no significant change in the inelastic spectrum was observed across the cubic-to-monoclinic distortion at approximately 190 K, consistent with a similar local structure in both phases with distortions induced by the central Cd tetrahedron.

D. Comparison with magnetization data

In Fig. 7 we compare the temperature dependence of the inverse magnetic susceptibility ($1/\chi$) calculated for the pentagonal CEF scheme with measurements performed on a magnetically diluted $Y_{0.95}Tb_{0.05}Cd_6$ sample. The magnetic dilution was done in order to minimize the influence of magnetic correlations between the Tb moments. Fits to the high temperature magnetization data yield an effective Tb moment of $9.4(1)\mu_B$, close to the theoretical effective Tb^{3+} moment of $9.72\mu_B$.

For the calculation of the magnetization and susceptibility, the full magnetic Hamiltonian includes both the CEF contribution and a Zeeman splitting term,

$$H = g_J \mu_B B J_{z'} + H_{\rm CEF}^{(5)} = g_J \mu_B B J_{z'} + B_2^0 O_2^0, \qquad (9)$$

where g_J is the Landé g factor ($g_J = 1.5$ for Tb^{3+}) and B is the externally applied magnetic field. We then calculate the total free energy $\mathcal{F}$, the magnetization ($M = -\partial\mathcal{F}/\partial B$), and the susceptibility ($\chi = -\partial^2\mathcal{F}/\partial^2 B$).

The CEF contribution, however, is written in terms of the local coordinate system (x,y,z) where the z axis points along the fivefold axes of the icosahedral cluster [30]. On the other hand, the Zeeman term is written in the laboratory frame (x',y',z'), where the z' axis points along the direction of the applied magnetic field. For these measurements, the magnetic field was applied along one of the crystallographic cubic axes, which is also the twofold axes of the icosahedral cluster [4,9]. For Tb moments directed along the fivefold axes of the Tsai-type clusters, we must consider the angles they subtend with the applied field for calculations of M and $1/\chi$ ($\theta = 31.72°$, $58.29°$, and $90°$). Taking this into account, we find very good agreement between the measured and calculated inverse susceptibility, confirming the moment direction for Tb^{3+} along the local pseudofivefold axis in the paramagnetic phase of $TbCd_6$ determined from the inelastic neutron scattering measurements of the CEF excitations.

IV. SUMMARY

We have performed inelastic neutron scattering measurements on powder samples of the quasicrystal approximant, $TbCd_6$, grown using isotopically enriched ^{112}Cd. Both quasielastic and distinct inelastic excitations were observed below 3 meV. The integrated intensity of the quasielastic scattering measured in the paramagnetic phase diverges as $T_N \sim 22$ K is approached from above. The inelastic scattering, and its evolution with temperature, are well characterized by

considering only the leading axial term, $B_2^0 O_2^0$, of the CEF Hamiltonian for local pentagonal symmetry for both the cubic and monoclinic phases. The good fit to our data using only this term indicates that the Tb moments in the paramagnetic phase are directed primarily along the unique local pseudofivefold axis of the Tsai-type cluster. Our results for $TbCd_6$ are also consistent with the CEF scheme [with $B_2^0 = -0.044(1)$ meV] determined via fitting low-temperature specific heat measurements on $Zn_{85.5}Sc_{11}Tm_{3.5}$, a 1/1 cubic approximant of the i-Zn-Sc quasicrystal, where a small amount of Tm^{3+} was substituted for Sc [30]. Finally, our conclusions are confirmed by a comparison between the inverse susceptibility determined from magnetization measurements using a magnetically diluted $Tb_{0.05}Y_{0.95}Cd_6$ sample, and that calculated using the CEF level scheme determined from the neutron measurements.

ACKNOWLEDGMENTS

We gratefully acknowledge the Institut Laue-Langevin, France for allocation of beam time and resources for this work, the assistance of S. Rolls during the measurements, and useful discussions with G. Beutier and R. J. McQueeney. Work at the Ames Laboratory was supported by the Department of Energy, Basic Energy Sciences, Division of Materials Sciences & Engineering, under Contract No. DE-AC02-07CH11358. Part of this study was carried out within the European C-MAC network.

[1] C. P. Gómez and S. Lidin, Phys. Rev. B **68**, 024203 (2003).
[2] S. Y. Piao, C. P. Gómez, and S. Lidin, Z. Naturforsch. **60b**, 644 (2006).
[3] A. I. Goldman, T. Kong, A. Kreyssig, A. Jesche, M. Ramazanoglu, K. W. Dennis, S. L. Bud'ko, and P. C. Canfield, Nat. Mater. **12**, 714 (2013).
[4] R. Tamura, Y. Muro, T. Hiroto, K. Nishimoto, and T. Takabatake, Phys. Rev. B **82**, 220201(R) (2010).
[5] M. G. Kim, G. Beutier, A. Kreyssig, T. Hiroto, T. Yamada, J. W. Kim, M. de Boissieu, R. Tamura, and A. I. Goldman, Phys. Rev. B **85**, 134442 (2012).
[6] A. Mori, H. Ota, S. Yoshiuchi, K. Iwakawa, Y. Taga, Y. Hirose, T. Takeuchi, E. Yamamoto, Y. Haga, F. Honda, R. Settai, and Y. Ōnuki, J. Phys. Soc. Jpn. **81**, 024720 (2012).
[7] T. Kong, S. L. Bud'ko, A. Jesche, J. McArthur, A. Kreyssig, A. I. Goldman, and P. C. Canfield, Phys. Rev. B **90**, 014424 (2014).
[8] T. J. Sato, Acta Crystallogr. **61**, 39 (2005).
[9] A. I. Goldman, Sci. Technol. Adv. Mater. **15**, 044801 (2014).
[10] C. Godrèche, J. M. Luck, and H. Orland, J. Stat. Phys. **45**, 777 (1986).
[11] R. Lifshitz, Phys. Rev. Lett. **80**, 2717 (1998).
[12] E. Y. Vedmenko, U. Grimm, and R. Wiesendanger, Phys. Rev. Lett. **93**, 076407 (2004).
[13] A. Jagannathan, Phys. Rev. Lett. **92**, 047202 (2004).
[14] S. Matsuo, S. Fujiwara, H. Nakano, and T. Ishimasa, J. Non-Cryst. Solids **334-335**, 421 (2004).
[15] S. Thiem and J. T. Chalker, Europhys. Lett. **110**, 17002 (2015).
[16] S. Thiem and J. T. Chalker, Phys. Rev. B **92**, 224409 (2015).
[17] A. P. Tsai, J. Q. Guo, E. Abe, H. Takakura, and T. J. Sato, Nature (London) **408**, 537 (2000).
[18] H. Takakura, C. Pay Gómez, A. Yamamoto, M. de Boissieu, and A. P. Tsai, Nat. Mater. **6**, 58 (2007).
[19] T. Yamada, H. Takakura, T. Kong, P. Das, W. T. Jayasekara, A. Kreyssig, G. Beutier, P. C. Canfield, M. de Boissieu, and A. I. Goldman, Phys. Rev. B **94**, 060103(R) (2016).
[20] P. C. Canfield and Z. Fisk, Philos. Mag. B **65**, 1117 (1992).
[21] P. C. Canfield and I. R. Fisher, J. Cryst. Growth **225**, 155 (2001).
[22] P. C. Canfield, T. Kong, U. S. Kaluarachchi, and N. H. Jo, Philos. Mag. **96**, 84 (2016).
[23] A. P. Tsai, Chem. Soc. Rev. **42**, 5352 (2013).
[24] R. Tamura, Isr. J. Chem. **51**, 1263 (2011).
[25] K. Nishimoto, T. Sato, and R. Tamura, J. Phys.: Condens. Matter **25**, 235403 (2013).
[26] D. Liu, Ph.D. dissertation, Université Grenoble Alpes, 2015.
[27] T. Ishimasa, Y. Kasano, A. Tachibana, S. Kashimoto, and K. Osaka, Philos. Mag. **87**, 2887 (2007).
[28] T. Yamada, H. Euchner, C. P. Gómez, H. Takakura, and M. de Boissiue, J. Phys.: Condens. Matter **25**, 205405 (2013).
[29] H Euchner, T. Yamada, S. Rols, T. Ishimasa, J. Ollivier, H. Schnober, M. Mihalkovic, and M. de Boissieu, J. Phys.: Condens. Matter **26**, 055402 (2014).
[30] S. Jazbec, S. Kashimoto, P. Koželj, S. Vrtnik, M. Jagodič, Z. Jagličić, and J. Dolinšek, Phys. Rev. B **93**, 054208 (2016).
[31] U. Walter, Phys. Rev. B **36**, 2504 (1987).
[32] U. Walter, Europhys. Lett. **4**, 1285 (1987).
[33] J. Jensen and A. R. Mackintosh, *Rare Earth Magnetism. Structures and Excitations* (Clarendon Press, Oxford, 1991).